

# TiO<sub>2</sub> Inverse Opals Fabricated Using Low-Temperature Atomic Layer Deposition\*\*

By Jeffrey S. King,\* Elton Graugnard, and Christopher J. Summers

Following the work of John<sup>[1]</sup> and Yablonovitch,<sup>[2]</sup> the study of photonic crystals (PCs) has become an important area of research for applications in optoelectronics and electromagnetics, as well as chemical and biological sensors. Formation of a complete photonic bandgap (PBG) requires a three-dimensional (3D) periodic structure exhibiting high refractive-index contrast. PCs based on infiltration of self-assembled opals are promising structures,<sup>[3–5]</sup> and a full PBG at infrared wavelengths has been produced in a silicon PC.<sup>[6,7]</sup> Also, transparent materials with indexes ranging from ~1.4 (SiO<sub>2</sub>) to 3.8 (Sb<sub>2</sub>S<sub>3</sub>) have been used to form inverse opals with pseudophotonic bandgaps (PPBGs) and potentially full PBGs in the visible-wavelength range.<sup>[8–12]</sup> Two-dimensional (2D) and 3D PC structures are being extensively modeled, and these studies show that changes in the structures, such as shifting the distribution of dielectric material, can significantly improve PBG properties. The importance of the precise placement of the dielectric material is demonstrated by the inverted “shell” structure, where the opal is infiltrated with a conformal shell-like coating, leaving small air pockets in the face-centered cubic (fcc) interstitial sites. For example, in a silicon inverse shell opal, the width of the PBG can be increased from 4.25 % to 8.6 %.<sup>[13]</sup> Similarly, the PBG width can also be increased to 9.6 % by formation of a non-close-packed structure.<sup>[14]</sup> Thus, the performance of these structures critically depends on precisely and accurately placed high-dielectric material, and the fabrication of these optimized structures will require a highly controllable infiltration method. Similarly, even for 2D and 3D photonic crystals not based on the opal architecture, highly controllable deposition methods will be imperative for maximizing desired photonic effects in real structures.

Atomic layer deposition (ALD) allows formation of low porosity, conformal films with submonolayer control.<sup>[15]</sup> These features make ALD ideal for infiltration, and we have successfully used the technique to create ZnS/Mn inverse opals.<sup>[16,17]</sup> A similar layer-by-layer method has also been demonstrated

to increase the mechanical stability and oxide-filling fraction of a SiO<sub>2</sub> opal using SiCl<sub>4</sub> and H<sub>2</sub>O precursors.<sup>[18]</sup> In this paper, we extend the ALD studies to TiO<sub>2</sub>, which has long been a candidate material for use in PCs because its refractive index (*n*) can exceed 2.8 and 2.65 ( $\lambda$  = 500 nm) for the rutile and anatase phases, respectively.<sup>[3,19–21]</sup> Unfortunately, the growth methods used to date have resulted in infiltration filling fractions of, at most, 50 % of the available pore volume. In addition, these opals were infiltrated either by solution precipitation or by nanoparticle co-sedimentation, neither of which offers much precision in placement of the high-dielectric material. Infiltration by ALD holds promise for attaining inverse shell opals that exhibit filling fractions very close to the optimum 90 % of the pore volume.

For this study, TiO<sub>2</sub> inverse opals were formed by ALD infiltration of silica opals. Opal templates with spheres sized between 200 and 440 nm in diameter were formed on silicon and quartz substrates by use of a confinement cell.<sup>[22]</sup> The resulting fcc 10  $\mu$ m thick opal films had the (111) planes parallel to the substrate. TiO<sub>2</sub>/SiO<sub>2</sub> infiltrated opals were formed next using a flow-style, hot-wall ALD reactor. From atomic force microscopy (AFM) studies of planar films grown in our ALD system, TiO<sub>2</sub> coatings yielded root-mean-square (RMS) roughness values of 0.2 nm at 100 °C, 2.1 nm at 300 °C, and 9.6 nm at 600 °C. Thus, to promote even filling and extremely smooth interfaces, very-low-temperature deposition is essential. However, deposition at 100 °C was also found to result in amorphous TiO<sub>2</sub>, whose refractive index is 2.35; this is significantly below that obtained in anatase or rutile films.<sup>[23]</sup> It was also found during this study that the formation of the inverse opal by etching the SiO<sub>2</sub> spheres requires crystalline TiO<sub>2</sub>; otherwise, HF etches the amorphous phase, destroying the sample. Therefore, we developed a technique that combined deposition at a low temperature with a subsequent heat treatment to promote formation of the anatase or rutile phase while maintaining good infiltration and smooth films. AFM studies showed an increase in RMS roughness of only 0.2 nm after conversion to anatase, resulting in a film roughness significantly lower than directly grown anatase. Attainment of 100 % rutile phase was difficult; however, the anatase phase of TiO<sub>2</sub> has a refractive index greater than 2.85 for wavelengths shorter than 400 nm,<sup>[21]</sup> and should allow formation of a full PBG for UV wavelengths, as well as show strong PPBGs in the visible-light range. Anatase also exhibits far less birefringence than rutile, which makes both theoretical and experimental analyses easier.

ALD growth was performed by alternating pulses of TiCl<sub>4</sub> and H<sub>2</sub>O precursors, each separated by a N<sub>2</sub> purge.<sup>[24]</sup> From planar-growth studies, a growth rate of ~0.98 Å per cycle was found for deposition at 100 °C. Since ALD is a highly conformal growth technique, 100 % infiltration is not possible, and small air pockets should remain in the fcc interstitial sites. Geometrical arguments show that the void space of the close-packed (111) planes will close when the coating thickness reaches 7.75 % of the sphere diameter, leaving the pore volume partially filled. After application of the necessary num-

[\*] Dr. J. S. King, Dr. E. Graugnard, Prof. C. J. Summers  
School of Materials Science and Engineering  
Georgia Institute of Technology  
Atlanta, GA 30332-0245 (USA)  
E-mail: jeffrey.king@mse.gatech.edu

[\*\*] This work was supported by the U.S. Army Research Office under MURI contract DAAD19-01-1-0603, and the Georgia Institute of Technology Molecular Design Institute under prime contract N00014-95-1-1116 from the Office of Naval Research. We also thank S. Blomquist and the U.S. Army Research Lab for assistance with preliminary ALD studies.

ber of pulse/purge cycles, the ALD reactor was heated to 400 °C and held for 2 h to convert the amorphous TiO<sub>2</sub> film to polycrystalline anatase. Prior to formation of the inverse opal by HF etching, an ion mill was used to remove the thin TiO<sub>2</sub> capping layer from the surface of the infiltrated opal, thus exposing the silica spheres and facilitating their removal. Following deposition, specular reflectance spectroscopy, transmission spectroscopy, and scanning electron microscopy (SEM) were used to characterize the structures.

SEM was used to confirm successful infiltration of the opal with TiO<sub>2</sub> and to examine the degree of conformality of the resulting films. Figure 1 shows SEM images of a 433 nm inverse opal. Figure 1a is an image of the (111) top plane of the opal, showing a cross-sectional view of the TiO<sub>2</sub> infiltration

layer. As previously discussed, ion milling facilitated removal of the top half of the first layer of spheres, allowing characterization of the film thickness and conformality. Figure 1b is a higher magnification image, and further illustrates the highly conformal nature of the film, shown by the presence of small air pockets between the air spheres. Figure 1c is an image of a fracture surface of a portion of the opal that has been cleaved. This image clearly shows that the silica spheres have been removed, leaving a “hollow” TiO<sub>2</sub> inverse shell opal. The dark spots on the spherical surfaces are the contact points where the spheres were connected prior to fracture.

The success of infiltration and etching can be followed by examining the shift of the  $\Gamma$ -L PPBG peak found in specular reflectance and transmission. This peak (reflectance) or dip (transmission) corresponds to Bragg diffraction from the (111) planes, and was measured at 15° from normal incidence for reflectivity and at normal incidence for transmission. Figure 2 shows the reflection spectra measured before infiltration, after ALD infiltration and heat treatment, and after etching during formation of a 266 nm inverse opal. The  $\Gamma$ -L

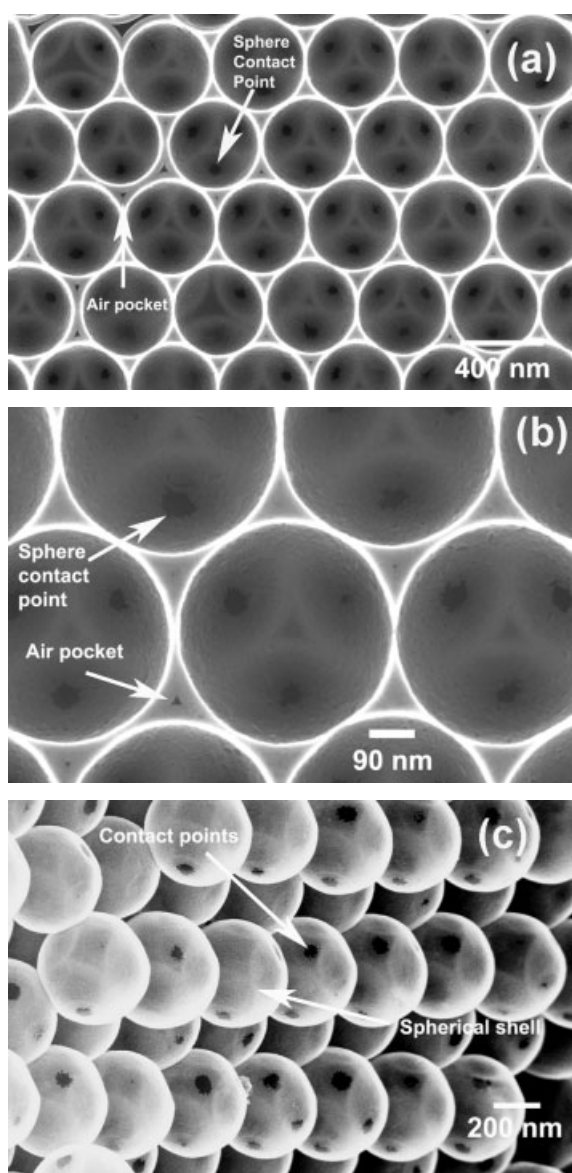


**Figure 1.** SEM images of 433 nm TiO<sub>2</sub> inverse opal. a) Ion-milled (111) surface, b) higher magnification ion-milled (111) surface, and c) fracture surface.

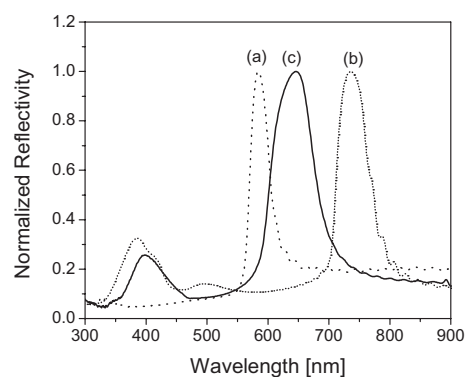


**Figure 2.** Reflectance spectra measured for 266 nm bare, infiltrated, and inverse opals (15° incidence). a) Bare opal, with 584 nm  $\Gamma$ -L PPBG peak, b) infiltrated opal, with 736 nm  $\Gamma$ -L PPBG peak, and c) inverse opal, with 646 nm  $\Gamma$ -L PPBG peak.

peak shifts from 584 nm to 736 nm after TiO<sub>2</sub> infiltration, consistent with an increase in the average dielectric constant of the opal, and indicating 88 % infiltration of the pore volume, as estimated from the Bragg equation adapted for opal structures. Formation of the inverse opal resulted in a shift of the  $\Gamma$ -L peak to 646 nm, consistent with a decrease in dielectric constant. The full width at half maximum (FWHM) of the reflectivity peak increased after both infiltration and inversion; from 37 nm for the bare opal, to 63 nm for the infiltrated opal, and to 82 nm for the inverse opal. These values represent peak-width-to-position ratios of 6.3 %, 8.5 %, and 12.8 %, respectively. It is more accurate to compare the calculated photonic band diagrams to the collected normal incidence transmission spectra, since reflectivity was collected at 15° from normal, slightly off the  $\Gamma$ -L direction. Since reflectivity measurements give information about the outermost layers of

the opal, while transmission measurements probe the full opal, any peak-broadening effects due to disorder in the structure are expected to be more pronounced in the transmission spectra. The FWHM of the transmission dip increased after both infiltration and inversion, from 42 nm for the bare opal, to 83 nm for the infiltrated opal, and to 104 nm for the inverse opal. These values yield peak-width-to-position ratios of 7.11 %, 11.3 %, and 16.1 %. While a rigorous comparison requires more extensive calculations that take into account the divergence of the measurement beam, which should broaden each peak, the values found from reflectivity and transmission agree well with the trend of increasing PPBG widths of 5.3 %, 6.43 %, and 15.7 % predicted from the calculated band diagrams. Comparison of the peak-width-to-position ratios reveals that the reflectivity spectra more closely agree with predicted gap widths, as expected. The positions of the transmission dips were 590 nm for bare opal, 736 nm for infiltrated opal, and 647 nm for inverse opal, also showing good agreement with the calculated band diagrams, which have PPBGs centered at 590 nm, 730 nm, and 637 nm, respectively.

In addition to the shift in the  $\Gamma$ -L peak, the development of higher-energy peaks was discovered. After infiltration, a reflectivity peak at 385 nm develops that is  $\sim 30$  % of the intensity of the  $\Gamma$ -L peak and is attributed to higher-energy band features. This peak shifts to 398 nm and decreases slightly in relative intensity in the inverse opal. For larger-sized opals, we have observed higher-order peaks that have intensities comparable to the  $\Gamma$ -L peak. The lower intensity of the high-energy peak for the 266 nm opal is attributed to increased absorption below 400 nm.

To demonstrate the control that ALD offers, a 266 nm opal was infiltrated in steps consisting of 20 pulse/purge cycles, and the transmission and reflectivity were measured after each infiltration step. Figure 3a shows the resulting reflectivity data from these measurements, and Figure 3b is an intensity plot of the same data, after interpolation, clearly showing the shift in the PPBG peaks. Figure 4a shows the resulting void-filling fraction as a function of number of ALD cycles, demonstrating the precision that can be achieved in deposition. Monte Carlo calculations show that the (111) plane will close at  $\sim 86$  % infiltration, as indicated in Figure 4a by the dashed line. While the experimental data clearly indicates that this maximum infiltration amount has been achieved by the 350th ALD cycle, it is also important to notice that no change in filling fraction occurs after the last 20 ALD cycles, indicating that access to the remaining porosity in the structure has been closed, as predicted. The data indicates a final filling fraction of 88 %, which is remarkably close to the 86 % predicted by simulation. Figure 4b shows the experimentally determined coating thickness as a function of ALD cycles. This data was calculated by comparing the resulting shifts in peak position after every 20 ALD growth cycles with the peak positions from calculated band diagrams for partially infiltrated shell opals. The slope of the trend line reveals a growth rate of 0.51 Å per cycle, approximately half that of the planar growth rate. This lower growth rate indicates that the interior surfaces

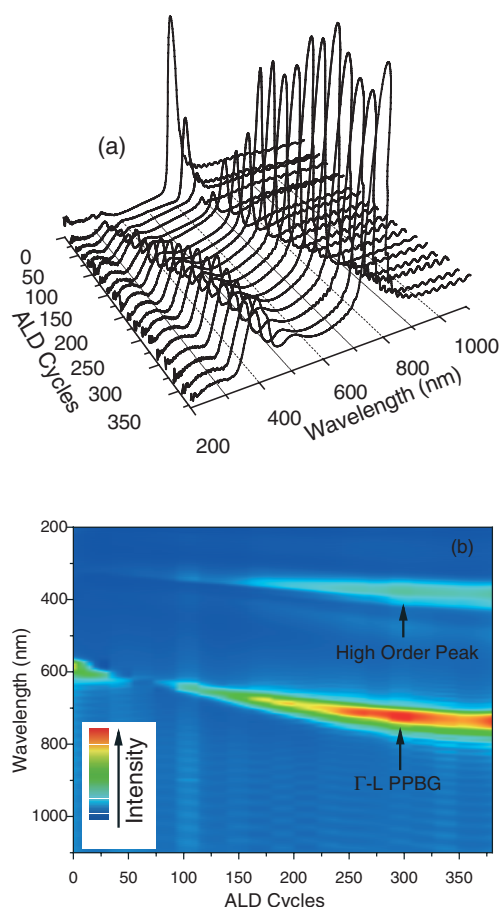


**Figure 3.** Reflectivity data from stepwise  $\text{TiO}_2$ -infiltrated 266 nm  $\text{SiO}_2$  opal. a) Measured spectra and b) interpolated intensity plot of wavelength versus ALD cycles, indicating the position of  $\Gamma$ -L PPBGs. Regions of high reflectivity are indicated by arrows.

are not reaching full saturation. In fact, the surface area in a 10  $\mu\text{m}$  thick 266 nm opal film is approximately 167 times that of the underlying planar area. Thus, although the coatings are uniform, the growth rate could be increased by further optimizing the ALD conditions.

In summary, we report the low-temperature fabrication of  $\text{TiO}_2$  inverse shell opals using ALD. Self-assembled 200 to 440 nm sized silica opals were infiltrated using conventional precursors at 100  $^\circ\text{C}$ , annealed for 2 h at 400  $^\circ\text{C}$ , and inverted using HF. The shifts in the  $\Gamma$ -L PBG position and width were confirmed by specular reflectance and transmission spectroscopy, revealing behavior consistent with photonic-band calculations. The peak positions indicate that filling terminated at  $\sim 88$  % of the pore volume, as estimated from the modified Bragg equation, supporting the theoretical prediction that maximum filling for a shell opal is 86 %. SEM and AFM analysis revealed ultra-smooth (RMS roughness of  $<0.5$  nm), highly conformal anatase films as a result of the combination of low-temperature deposition with a short heat treatment. In addition, precise infiltration control ( $<1$  nm) was achieved with this technique, making the fine-tuning of photonic crystal

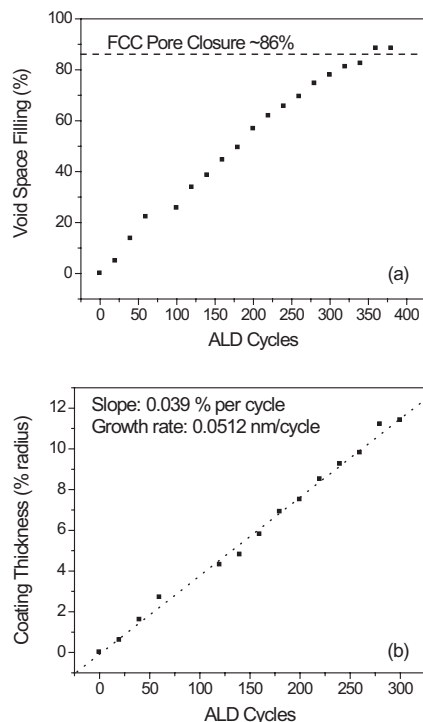


**Figure 4.** Stepwise-infiltration calculations for a 266 nm opal, including a) void-space filling fraction and b) coating thickness as a function of ALD cycles.

properties a reality. The success of this work shows that precisely controlling the placement of dielectric materials is possible using ALD, enabling the fabrication of many of the “optimized” structures that have been predicted to have the best optical properties. The digital nature of ALD growth has been demonstrated to allow angstrom-scale fine-tuning of complex structures, and since it can be used to deposit metals, insulators, and semiconductors, many different structures can be fabricated.

## Experimental

Monodisperse silica colloids were formed using the Stober method and dispersed in ultrapure deionized (DI) water [25]. Silica opals were next grown by forced sedimentation in a confinement cell [22]. After sintering the opal films in air at 800 °C for 2 h, TiO<sub>2</sub> was grown within the opal using alternating 4 s pulses of TiCl<sub>4</sub> and H<sub>2</sub>O, each separated by a 10 s, 225 sccm N<sub>2</sub> purge, while maintaining the substrate at 100 °C. The vacuum level within the reactor was ~500 mtorr (67 Pa) during pulses, and 200 mtorr (27 Pa) during purges. The precursor gases, derived from room-temperature liquid sources, were introduced to a N<sub>2</sub> carrier gas using computer-controlled solenoid valves. Post-deposition heat treatment was performed in the atomic layer deposition (ALD) reactor with constant N<sub>2</sub> flow of 225 sccm. The surface of the heat-treated opal was next ion milled for several minutes with a 4 keV Ar<sup>+</sup> beam at 15° incidence. To remove the silica spheres, a drop of 2 % HF solution was placed on the ~3 mm diameter milled region. After 15 min, the surface was rinsed with DI water and dried in an oven at 110 °C. This was repeated 3 times (a total of 45 min) to fully remove the silica spheres.

All scanning electron microscopy (SEM) images were acquired using a LEO 1530 SEM. Reflectivity and transmission measurements were performed using a Beckman DU640 spectrophotometer. Surface roughness was calculated from images acquired using a Park Scientific Instruments Autoprobe CP atomic force microscope operating in contact mode. Photonic-band diagrams were calculated by the plane-wave expansion method using the MIT Photonic Bands program.

Received: April 29, 2004

Final version: November 17, 2004

- [1] S. John, *Phys. Rev. Lett.* **1987**, *58*, 2486.
- [2] E. Yablonovitch, *Phys. Rev. Lett.* **1987**, *58*, 2059.
- [3] J. E. G. J. Wijnhoven, W. L. Vos, *Science* **1998**, *281*, 802.
- [4] H. M. Yates, W. R. Flavell, M. E. Pemble, N. P. Johnson, S. G. Romanov, C. M. Sotomayor-Torres, *J. Cryst. Growth* **1997**, *170*, 611.
- [5] S. G. Romanov, H. M. Yates, M. E. Pemble, R. M. De La Rue, *J. Phys.: Condens. Matter* **2000**, *12*, 8221.
- [6] A. Blanco, E. Chomski, S. Grabtchak, M. Ibisate, S. John, S. W. Leonard, C. Lopez, F. Meseguer, H. Miguez, J. P. Mondla, G. A. Ozin, O. Toader, H. M. van Driel, *Nature* **2000**, *405*, 437.
- [7] Y. A. Vlasov, X.-Z. Bo, J. C. Sturm, D. J. Norris, *Nature* **2001**, *414*, 289.
- [8] R. C. Schroden, M. Al-Daous, A. Stein, *Chem. Mater.* **2001**, *13*, 2945.
- [9] M. Muller, R. Zentel, T. Maka, S. G. Romanov, C. M. S. Torres, *Adv. Mater.* **2000**, *12*, 1499.
- [10] S. G. Romanov, A. V. Fokin, R. M. De La Rue, *Appl. Phys. Lett.* **1999**, *74*, 1821.
- [11] A. Blanco, H. Miguez, F. Meseguer, C. Lopez, F. Lopez-Tejiera, J. Sanchez-Dehesa, *Appl. Phys. Lett.* **2001**, *78*, 3181.
- [12] B. H. Juarez, M. Ibisate, J. M. Palacios, C. Lopez, *Adv. Mater.* **2003**, *15*, 319.
- [13] S. John, K. Busch, *J. Lightwave Technol.* **1999**, *17*, 1931.
- [14] M. Doosje, B. J. Hoenders, J. Knoester, *J. Opt. Soc. Am. B* **2000**, *17*, 600.
- [15] M. Ritala, *Appl. Surf. Sci.* **1997**, *112*, 223.
- [16] J. S. King, C. W. Neff, C. J. Summers, W. Park, S. Blomquist, E. Forsythe, D. Morton, *Appl. Phys. Lett.* **2003**, *83*, 2566.
- [17] J. S. King, C. W. Neff, S. Blomquist, E. Forsythe, D. Morton, C. J. Summers, *Phys. Status Solidi B* **2004**, *241*, 763.
- [18] H. Miguez, N. Tetreault, B. Hatton, S. M. Yang, D. Perovic, G. A. Ozin, *Chem. Commun.* **2002**, 2736.
- [19] G. Subramania, K. Constant, R. Biswas, M. M. Sigalas, K.-M. Ho, *Appl. Phys. Lett.* **1999**, *74*, 3933.
- [20] E. D. Palik, G. Ghosh, *Handbook of Optical Constants of Solids*, Academic, San Diego, CA **1998**.
- [21] S. Tanemura, L. Miao, P. Jin, K. Kaneko, A. Terai, N. Nabatova-Gabain, *Appl. Surf. Sci.* **2003**, *212–213*, 654.
- [22] S. H. Park, D. Qin, Y. Xia, *Adv. Mater.* **1998**, *10*, 1028.
- [23] J. Aarik, A. Aidla, T. Uustare, V. Sammelselg, *J. Cryst. Growth* **1995**, *148*, 268.
- [24] M. Ritala, M. Leskela, E. Nykanen, P. Soininen, L. Niinisto, *Thin Solid Films* **1993**, *225*, 288.
- [25] W. Stober, A. Fink, E. Bohn, *J. Colloid Interface Sci.* **1968**, *26*, 62.